Titre: Title:	Multiscale insights into Sliding Surface Liquefaction through DEM simulations
Auteurs: Authors:	Manuel Cárdenas-Barrantes, & Carlos Ovalle
Date:	2025
Type:	Article de revue / Article
Référence: Citation:	Cárdenas-Barrantes, M., & Ovalle, C. (2025). Multiscale insights into Sliding Surface Liquefaction through DEM simulations. Computers and Geotechnics, 183, 107191 (11 pages). https://doi.org/10.1016/j.compgeo.2025.107191

Document en libre accès dans PolyPublie
Open Access document in PolyPublie

URL de PolyPublie: PolyPublie URL:	https://publications.polymtl.ca/63420/
Version:	Version officielle de l'éditeur / Published version Révisé par les pairs / Refereed
Conditions d'utilisation: Terms of Use:	Creative Commons Attribution 4.0 International (CC BY)

Document publié chez l'éditeur officiel
Document issued by the official publisher

Titre de la revue: Journal Title:	Computers and Geotechnics (vol. 183)
Maison d'édition: Publisher:	Elsevier BV
URL officiel: Official URL:	https://doi.org/10.1016/j.compgeo.2025.107191
Mention légale: Legal notice:	© 2025 The Authors. Published by Elsevier Ltd. This is an open access article under the CC BY license (http://creativecommons.org/licenses/by/4.0/)

Research paper

Multiscale insights into Sliding Surface Liquefaction through DEM simulations

Manuel Cárdenas-Barrantes [ID], Carlos Ovalle [ID] *

Department of Civil, Geological and Mining Engineering, Polytechnique Montreal, Montreal, Quebec, Canada
Research Institute on Mines and the Environment (IRME), Polytechnique Montreal, Quebec, Canada

ARTICLE INFO

ABSTRACT

Recognizing the mechanisms that trigger liquefaction is critical for developing reliable models to prevent landslides. The tendency for liquefaction to occur generally decreases with increasing soil density. However, when grain fragmentation occurs, the material becomes more contractive, making liquefaction possible even in relatively dense samples. This phenomenon was first recognized and named Sliding Surface Liquefaction (SSL) by Kyoji Sassa's research group (*Soils Found*, a=Vol 36, 1996, pp.53-64), who reported comprehensive laboratory studies on the topic. Yet, the mechanisms at the grain scale remain poorly understood. To advance in the understanding of SSL and support the development of predictive models, we investigate the links between micro- and macromechanical behavior in crushable granular materials subjected to constant volume shearing. We perform two-dimensional simulations using the Contact Dynamics Discrete Element Method, focusing on the effects of particle fragmentation strength and grading evolution during undrained shearing until liquefaction. The results reveal that higher densities and particle strength delay the onset of liquefaction. At high densities, regardless of the strength of the particles, grading during crushing asymptotically approaches an ultimate distribution, which depends on the initial density and is not associated with the occurrence of liquefaction. Although the amount of grain fragmentation is lower in looser samples, liquefaction occurs in earlier stages than in denser cases.

1. Introduction

Understanding the physics at the origin of landslides is crucial to improve methods for predicting and minimizing these catastrophic events. To do so, field observations and laboratory test results are typically used to develop analytical and numerical models based on macromechanical observations (i.e., at the scale of the material's elementary volume). However, since geomaterials are inherently discrete media, their behavior is governed by local mechanisms at the interparticle scale (i.e., the micromechanical scale). Therefore, the development of physical models must be based on multiscale considerations, which require a deep understanding of the connections between different scales.

Landslides can be triggered by numerous mechanisms, including diffuse failure of soils (Daouadji et al., 2011), rainfall-induced motion (Zhou et al., 2022; Alonso, 2021), internal erosion (Hu et al., 2018), suffusion (Yang et al., 2019) and liquefaction of loose, saturated sandy material (Ishihara, 1996). Liquefaction is typically defined as the loss of shear resistance in granular materials subjected to undrained shearing. This phenomenon is observed in loose saturated soils under

rapid loading, followed by an increase in pore pressure and, consequently, the vanishing of the effective stresses. It is well-known that the liquefaction occurs in loose granular soils. However, relatively dense samples may also exhibit excess pore pressure if grain fragmentation occurs (Lade et al., 1996; Kikumoto et al., 2010; Hyodo et al., 2017; Kokusho et al., 2004). In fact, experimental evidence suggests that even relatively dense sands may liquefy when grain crushing is significant (Sassa et al., 2004; Wang and Sassa, 2000). This phenomenon, known as Sliding Surface Liquefaction (SSL) (Sassa et al., 1996), has been identified as a potential mechanism initiating rock avalanches (Yan et al., 2023) and rapid landslides in loess (Hong et al., 2021; Peng et al., 2018), urban landfills (Yin et al., 2016), mine rock waste dumps (Hawley and Cunning, 2017; Dawson et al., 1998), fault breccia (Cui et al., 2021) and pumice soils (Wang et al., 2002), among others.

SSL can be understood within the framework of the critical state theory. The critical state void ratio is known to decrease when particle crushing occurs, as the formation of finer particles leads to a more efficient packing arrangement (Lade et al., 1996; Biarez and Hicher,

---

* Correspondence to: 2500 Chem. de Polytechnique, Montréal, QC H3T 0A3, Canada.
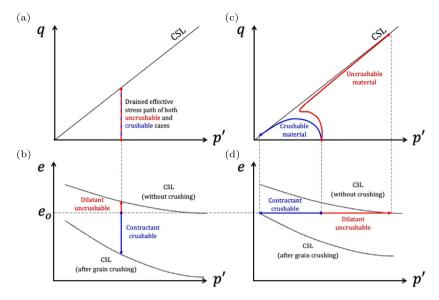*E-mail addresses:* manuel.cardenas@polymtl.ca (M. Cárdenas-Barrantes), carlos.ovalle@polymtl.ca (C. Ovalle).

Fig. 1. Critical state framework of uncrushable and crushable conceptual scenarios: (a) drained stress paths, (b) dilatancy, contractancy and CSLs for the drained cases, (c), undrained stress paths, and (d) undrained dilatancy and contractancy.

1997; Ovalle et al., 2015). Consequently, grain crushing shifts the critical state line (CSL) downward, reducing dilatancy in dense soils and potentially causing a contractant response (Kikumoto et al., 2010; Ovalle and Hicher, 2020; Wood et al., 2009). This conceptual behavior is illustrated in Fig. 1(a) for a drained shearing stress path at constant mean pressure (p') and increasing deviatoric stress (q). For a dense soil with an initial void ratio e_o (i.e., below the CSL, see Fig. 1(b)), two scenarios arise: (i) if the material is uncrushable or experiences negligible grain crushing at the given stress levels, the $e - p'$ path exhibits dilation (shown in red in Fig. 1(b)); (ii) if the material undergoes grain crushing, the CSL shifts downward, leading to a contractant path (depicted in blue in Fig. 1(b)). Similarly, Fig. 1(c) presents the schematic response of the same dense material under undrained (i.e., constant volume) shearing; the behaviors are the following (see Fig. 1(c) and (d)): (i) for uncrushable material, the effective stress path is dilatant, generating negative excess pore pressure; (ii) for crushable material, the CSL moves downward, resulting in a contractant effective stress path. It is worth noting that, while the CSLs of the uncrushable scenarios are the same in Fig. 1(b) and (d), the CSL shift due to grain crushing is more pronounced in the drained case compared to the undrained case, since the lower effective stress level in the contractant undrained scenario leads to less amount of grain crushing. Also, note that the CSL positions in the figures are exaggerated to illustrate an extreme conceptual case, where a dilatant soil could transition to a highly contractant and potentially liquefiable state (i.e., loss of strength) due to grain crushing. Indeed, the extent of the CSL shift towards contractancy depends on the initial density and susceptibility to grain crushing, which is influenced by stress levels and particle fragmentation strength.

SSL has been observed in large-strain, constant-volume ring shear tests (Sadrekarimi and Olson, 2010; Sassa et al., 2004; Okada et al., 2004; Wang and Sassa, 2000), where particle fragmentation leads to strength weakening and liquefaction. Following these observations, some studies have proposed continuous constitutive models to predict SSL-triggered landslides (Gerolymos and Gazetas, 2007; Chen and He, 2020; Deng et al., 2023; Wang and Wang, 2022). Recent studies have focused on multiscale analyses of undrained shearing of crushable materials using the Discrete Element Method (DEM) (de Bono and McDowell, 2018; Shi et al., 2022). In these cases, grain fragmentation has been simulated using the particle replacement method (Åström and Herrmann, 1998), which employs an Apollonian fragment distribution to artificially generate a fractal grain size distribution. In addition, these studies generally focused on triaxial shearing tests with relatively

low shear strains and did not simulate liquefaction. Therefore, the mechanics underlying SSL at the particle scale remain poorly understood. In particular, the effects of particle crushing strength and mean pressure at the micromechanical scale have not been deeply analyzed. Moreover, it is not clear how fragmentation progresses towards an ultimate grain size distribution, which has been observed empirically (Coop et al., 2004; Sammis et al., 1986; Turcotte, 1986), could set a limit to the path to liquefaction.

In an extreme climate change scenario, soil and rock weathering degradation can be accelerated by more extreme wetting-drying (Oldecop and Alonso, 2004; Osses et al., 2021) or freeze-thaw cycles (Ishikawa and Miura, 2011), increasing the probability of SSL-triggered landslides. To prevent such events, a better understanding of the SSL mechanisms is essential to develop more reliable physics-based models and improve failure predictions. This paper presents a numerical multiscale analysis of the SSL mechanism. The main objective is to evaluate the effects of the material crushability in sheared granular media under constant volume. We perform virtual tests on samples composed of disks, simulating grain fragmentation through the bonded cell method implemented in a DEM model. The evolution of the microstructure is tracked to identify the microscopic mechanisms leading to macroscopic liquefaction, and the mechanical behavior is analyzed in relation to the evolution of particle grading upon crushing until reaching an ultimate distribution.

The manuscript is organized as follows. Section 2 describes the numerical approach used to create two-dimensional virtual assemblies of crushable particles and to shear them under constant volume at large strain. Section 3 presents the macromechanical behavior observed in the numerical tests and identifies the onset of liquefaction. Section 4 discusses microstructural descriptors to characterize the effects of the initial sample density and particle fragmentation strength on grain connectivity. Section 5 analyzes the evolution of particle grading due to crushing. Finally, Section 6 concludes and raises perspectives on this work.

2. Methodology and numerical set up

We performed two-dimensional constant-volume shear numerical tests on granular configurations of crushable particles with varying fragmentation strengths and sample density conditions. By imposing constant volume through the implementation of periodic boundary conditions during a shear test, we emulate the undrained state of

saturated soils under rapid loading, bypassing the need to simulate pore pressure and allowing us to compute effective stresses directly. This approach is analogous to laboratory constant volume tests in simple shear, where undrained conditions are imposed by keeping the sample height constant during shearing (ASTM, 2019). Regarding numerical tests, Zhang and Rothenburg (2020) compared the undrained behavior of granular materials using the constant volume approach and fluid-coupled DEM, and showed that the behaviors are equivalent.

The simulations were conducted using the Contact Dynamics (CD) method, a non-smooth implicit approach that solves the equations of motion for rigid grains. The contact forces and particle velocities are solved iteratively using a non-linear Gauss–Seidel algorithm (Radjai, 2008; Dubois et al., 2018). Unlike other methods, the CD framework does not require regularization parameters at particle interactions, such as contact stiffness or damping. Thus, it allows larger time steps and ensures unconditional stability, making it suitable to model the complex problem of soil crushability with few parameters. We used the open-source software LMGC90 (Dubois and Jean, 2003; Dubois et al., 2011) for these simulations.

The samples have a total of $2 \cdot 10^3$ crushable particles. The particles were deposited sequentially and geometrically layer by layer in a square box (Voivret et al., 2007), reaching a height (h) of $h/d_{max} \approx 36$, where d_{max} is the coarsest grain. To avoid crystallization and ordering effects, the grain size polydispersity was set as $d_{min}/d_{max} = 0.7$, where d_{min} is the finest grain. The geometry of each crushable particle was represented as a meshed disk using the software NEPER (Quey et al., 2011). In NEPER, each particle was randomly divided into similarly sized polygonal cells using a centroidal Voronoi tessellation (Du et al., 1999; Cantor et al., 2022). The method divides the grain surface on the basis of a set of generator points, which serve as the centroids of the cells. Each point in space is assigned to the Voronoi cell of its nearest generator point. To capture the effect of size on particle strength due to the increased probability of weak microcracks as particle size increases (Ovalle and Dano, 2020), we applied a constant cell density $\rho_{cell} = \frac{88}{\pi d_{max}^2}$ [cells per unit area]; the value was arbitrarily chosen to avoid an excessive number of fragments and keep computational time reasonable. This approach ensures that larger particles contain more potential fragmentation planes. Given the nature of the discretization of this particle, the number of cells in each particle is approximated to the nearest integer to maintain a density close to ρ_{cell}. The number of cells for the coarsest particles with d_{max} is 22, while for the smallest grains with diameter d_{min} is 9 cells. Including cells, each sample has more than $20 \cdot 10^3$ distinct elements. Fig. 2(a) illustrates examples of tessellations for both the smallest and the largest disks.

Cells within each crushable particle are bonded using a modified Mohr–Coulomb contact law. This law incorporates a normal cohesion (σ_c), representing the particle's strength, alongside a static friction coefficient (μ) (Radjai, 2008; Huillca et al., 2021). The bonds between cells are fractured if the stress exceeds the normal cohesion. When the yield criterion is met and the bond between cells breaks, the contact law changes to a standard Mohr–Coulomb dry friction law, identical to that used for interactions between separate crushable particles. To simulate various fragmentation scenarios and assess the impact of particle strength, we tested several levels of cohesive stress, ranging from $\sigma_c = 2.0 \cdot 10^3$ to $1.0 \cdot 10^4$ [kPa].

Uniaxial compression was applied in the vertical direction at a constant pressure $P_0 = 10$ [kPa], with gravity set to zero. To allow for large deformations during shearing, periodic boundary conditions were imposed on the lateral borders, so particles that reached one side reappeared on the opposite side (see Fig. 2(b)). Three initial friction coefficients ($\mu_0 \in [0.01, 0.20, 0.40]$) were used during the compaction phase to generate samples with distinct initial void ratios, $e \in [0.212, 0.225, 0.235] \pm 0.08$ (dense, medium-loose and loose, respectively), where e is defined as the ratio of the void area to the solid area. Previous works on two-dimensional DEM simulations have shown that
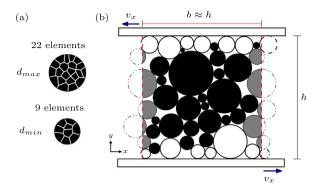

Fig. 2. (a) Example of tessellations for the largest and smallest disks used to represent crushable particles. Larger particles containing more cells due to their increased likelihood of fragmentation. (b) Boundary conditions scheme for shearing tests: Red dashed lines indicate the periodic boundary on the vertical axes. White particles are uncrushable and are attached to the walls to emulate wall roughness.

Table 1
Simulation parameters.

Parameter	Symbol	Value
Particle density	ρ	$2.7 \cdot 10^3$ kg m^{-2}
Maximum crushable particle diameter	d_{max}	1.0 m
Minimum crushable particle diameter.	d_{min}	$0.7 \, d_{max}$
Width and height of the box, x-axis periodic condition	h, b	$36.0 \, d_{max}$
Cell density	ρ_{cell}	28.01 m^{-2}
Number of particles	N	$2 \cdot 10^3$
Number of cells	N_{cell}	$\sim 20 \cdot 10^3$
Upper and lower wall speed	v_x	$5 \cdot 10^{-3}$ s^{-1} d_{max}
Shear rate	$\dot{\gamma}$	$1.4 \cdot 10^{-4}$ s^{-1}
Inertial number	I	$\simeq 0.6 \cdot 10^{-4}$

$e = 0.2$ represents a very dense packing (Voivret et al., 2007; Radjai et al., 1996), while loose contractant undrained behavior is obtained with void ratios around 0.25 (Wei, 2022; Deng et al., 2021). The compaction ended when the relative change in kinetic energy (K) fell below 10^{-3} ($\frac{K_t - K_{t+1}}{K_t} < 10^{-3}$), indicating mechanical stability. Less than 0.1% of the particles fractured at the lowest cohesion during the initial compaction.

Following the initial compaction, the friction coefficient was set to $\mu = 0.4$ for all cases. To maintain a constant volume, only horizontal movement was allowed on the upper and lower walls, restricting their movement along the vertical axis. Then a quasistatic shear test was carried out by horizontally displacing the upper and lower walls at a constant speed $v_x = 5 \cdot 10^{-3}$ s^{-1} d_{max}. To prevent strain localization at the boundaries, uncrushable particles were bonded to the upper and lower walls, creating artificial roughness that improves shear transmission (see Fig. 2(b)). Quasi-static conditions were maintained by ensuring that the inertial number $I = \dot{\gamma} d / \sqrt{P_0 / \rho}$ stayed below 10^{-4}, with the shear rate $\dot{\gamma} = v_x / h$, d the mean particle diameter, and ρ the particle density (Bruno Andeotti and Pouliquen, 2013). The physical and geometric parameters used in the simulations are summarized in Table 1. Fig. 3 shows different strain stages and their level of fragmentation for a dense sample ($e = 0.212$) with $\sigma_c = 0.5 \cdot 10^3 P_0$. For each test, the stress–strain states and the particle size distribution evolution upon shearing and crushing were tracked and analyzed, as presented in the following sections.

3. Macromechanical behavior

Constant volume shearing conditions in granular soils limit macroscopic dilation and contraction. This constraint forces structural reorganization of the grains, leading to significant changes in the microstructure. These changes can result in drastic variations in the effective stresses, which increase in dilative soils but may decrease
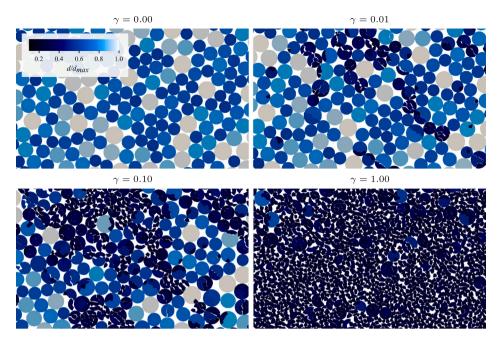
Fig. 3. Different stages of strain in a granular configuration sheared at $e = 0.212$ (dense case) with $\sigma_c = 0.5 \cdot 10^3 P_0$. Colors, ranging from dark blue to light blue, represent particle sizes scaled by d_{max}.
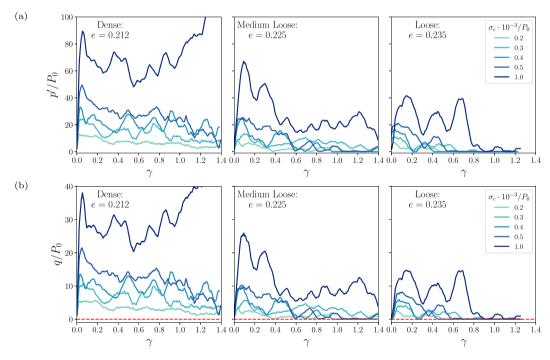

Fig. 4. (a) Mean and (b) deviatoric stress scaled by the initial compaction pressure as a function of the shear strain for three different densities and five levels of particle fragmentation strength. The dashed red line signals shear resistance equals to zero, $q = 0$.

until liquefaction in contractive ones. Furthermore, shearing stresses can induce particle fragmentation, which promotes further contractive behavior and, consequently, a further decrease in effective stresses. This evolution of stresses and microstructure can be captured with micromechanical detail using DEM models, through the granular stress tensor computed as:

$$\sigma_{\alpha\beta} = \frac{1}{V} \sum_{\forall c} f_\alpha^c \ell_\beta^c \,, \tag{1}$$

where α and β iterate over the x and y components, f_α^c is the α-component of the contact force at contact c, ℓ_β^c is the β-component of the vector joining the centers of mass of the particles interacting

at contact c, and V is the sample volume (Bathurst and Rothenburg, 1988). The mean effective stress is then given by $p' = (\sigma_1' + \sigma_2')/2$, where σ_1' and σ_2' are the principal effective stress values, and the deviatoric stress as $q = (\sigma_1' - \sigma_2')/2$.

Fig. 4(a) and (b) display the stress strain behavior of all the tests, in terms of the normalized mean (p'/P_0) and deviatoric (q/P_0) stresses, and the shear strain ($\gamma = \Delta x/h$, where Δx is the displacement in the x direction). Due to grain fragmentation events, the behaviors show substantial variations in stresses in all samples studied. Nonetheless, all tests exhibit initial hardening (i.e., increasing q and p') in a small strain range up to 0.05, approximately. The peak deviatoric stress
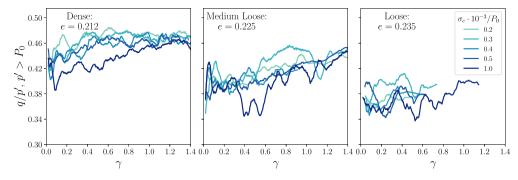
Fig. 5. Mobilized stress ratio (q/p') as a function of the shear strain for three different densities and five levels of particle fragmentation strength.

observed is directly proportional to both the sample density and the grain crushing strength. Hardening is followed by strain softening at large strain, except for the dense case ($e = 0.212$) with the strongest grains ($\sigma_c = 1.0 \cdot 10^3 P_0$), which presents limited softening until $\gamma = 0.6$ and then significant hardening due to the dilatant-like behavior with increasing effective stresses. Defining liquefaction as a complete loss of macromechanical shear resistance (i.e., $q = 0$), we observe that none of the dense samples with strain softening liquefied. In contrast, regardless of the strength of the particle fragmentation, all the loose cases ($e = 0.235$) liquefied and only one medium-loose sample ($e = 0.225$) did not. This sample exhibited a peak value of $q/P_0 \approx 20$ and softening until $q/P_0 \approx 10$, similar to the dense case at $\sigma_c = 0.5 \cdot 10^3 P_0$.

Fig. 5 displays the mobilized stress ratio q/p' throughout shearing, excluding data after liquefaction (i.e., considering only the ranges where $p' > P_0$). q/p' at large strains corresponds to the normalized resistance at critical state. All dense samples exhibit an increase q/p', stabilizing at approximately $q/p' \approx 0.46$. For medium-loose cases, normalized resistance continuously increases, reaching a mobilized ratio of around $q/p' \approx 0.45$ at higher strains. In contrast, the loose cases are only shown at lower strains because they subsequently liquefied and exhibit $q/p' \leq 0.40$. The observed decrease in the normalized critical resistance with density is due to the evolution of the particle shape after fragmentation. As explained below, the amount of particle crushing increases with the density of the samples, resulting in more fragmented angular grains (see Fig. 3) and therefore contributes to higher macromechanical resistance (Carrasco et al., 2023).

4. Microstructure and connectivity

In the liquefied samples, most microstructural integrity was lost as the contact network collapsed, leading to a transition from solid-like to liquid-like behavior. Fig. 6 shows the contact network at four different strain levels for loose samples with particles having a crushing strength of $\sigma_c = 0.5 \cdot 10^3 P_0$. Early in the test (i.e., at $\gamma = 0.1$ and 0.2), distinct force chains of strong contacts (red, representing forces above the mean value) and weak contacts (black, for forces below the mean value) are observed, aligning at a characteristic 45-degree angle under the simple shearing stress path. These force chains percolate from the bottom to the top of the sample, maintaining its mechanical stability. However, as shearing continues (i.e., at $\gamma = 0.4$ and 1.0), some strong force chains collapse due to particle crushing and rearrangement, leaving only dispersed weak force chains unable to support system stability, ultimately leading to liquefaction.

In the analysis of the robustness of the contact network (or connectivity), the mechanical coordination number (Z_M) serves as a crucial parameter. Defined as the mean number of contacts per particle, excluding rattlers (particles with zero or only one contact), Z_M reflects the stability of the structural integrity of the grain assembly. Fig. 7 shows Z_M for the three void ratios studied. As observed with mean and deviatoric stresses, Z_M shows maximum values directly proportional to the sample density and grain fragmentation strength. Regardless of the

σ_c, Z_M remains reasonably constant and did not experience significant drops in the cases that did not liquefy; namely, all dense cases and the case having the strongest grains ($\sigma_c = 1.0 \cdot 10^3 P_0$) in the medium dense case. In contrast, sudden drops in Z_M indicate a progressive weakening of the contact network during shearing, ultimately leading to collapse and a transition to a liquefied state. This leads to a reduction in contacts per particle, approaching characteristic values of a granular flow. This trend can be explained by the fact that loose packed systems do not exhibit contact redundancy, reflected in a lower coordination number. A lower Z_M reduces the possible load redistribution pathways during shear, making the system more prone to collapse. As a result, particles continue losing contacts due to their rearrangement into a more fluid-like state. In contrast, a high Z_M allows the load to be redistributed more effectively along multiple contacts and pathways, reducing the likelihood of network failure and thus preventing liquefaction.

The particle connectivity is further characterized by analyzing the probability of contacts, p_c, which represents the probability that a particle has exactly c contacts ($c \in [0, 1, 2, 3, 4, 5, 6, \ldots]$). Fig. 8 shows p_c as a function of shear strain for up to six contacts at a fragmentation strength of $\sigma_c = 0.5 \cdot 10^3 P_0$. Returning to Z_M at the onset of shear, it is inferred that particles with three and four contacts must constitute the highest probabilities, which is indeed the case, together accounting for more than 60% of the total contacts. In dense packing, the probability of having three and four contacts increases with strain, while the probabilities of having a different number of contacts remain stable. On the contrary, in the loose case, after reaching a peak, p_3 and p_4 remain constant while the probability of having zero and one contact increases (i.e., p_0 and p_1). Since the system is relatively loose, the newly formed fragments remain more mobile and establish fewer contacts, eventually becoming floating particles or rattlers. Consequently, the probabilities p_0 and p_1 continue to increase, while p_3 and p_4 decrease, as larger particles lose contacts due to fragment loss and the increased availability of local space. These observations are general for different σ_c, as shown in Fig. 9, which shows the evolution of (a) p_4 and (b) the probability of rattlers ($p_0 + p_1$) as a function of the shear strain.

Regarding the stability of the contact network, the redundancy number (i_r) is a well-known descriptor of the inter-particle contact behavior in a particle packing under shear loading (Pouragha and Wan, 2016; Kruyt, 2010), and thus an excellent indicator to assess liquefaction. In simple terms, i_r is the ratio between the degrees of freedom of the system and the number of constraints, defined as:

$$i_r = \frac{N_c \left(2 - \frac{N_s}{N_c}\right)}{3N \left(1 - \frac{N_r}{N}\right)}, \tag{2}$$

with N_c the total number of contacts, N_s the number of sliding contacts, N the number of particles, and N_r the number of rattlers (Pouragha and Wan, 2016). In this context, a sliding contact occurs when two particles in contact have a nonzero relative velocity. A sample reaches static equilibrium when $i_r = 1$. In hyperstatic states ($i_r > 1$), the system is mechanically stable and exhibits solid-like
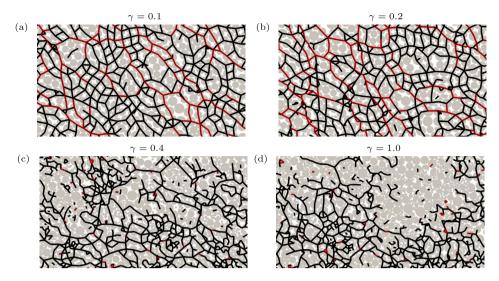
Fig. 6. Contact network at different strain levels in loose samples ($e = 0.235$) with a crushing strength of $\sigma_c = 0.5 \cdot 10^3 P_0$. Weak contacts, defined as those with force magnitudes below the instantaneous mean value, are shown in black, while strong contacts, with force magnitudes above the mean, are shown in red.
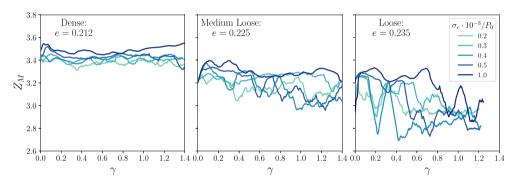

Fig. 7. Mechanical coordination number as a function of the shear strain for three different densities and five levels of particle fragmentation strength.
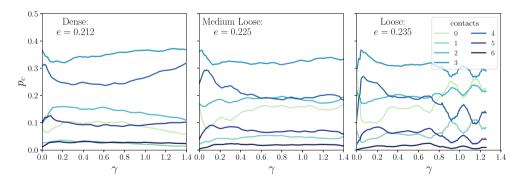

Fig. 8. Probability of contacts as a function of the shear strain for three different densities and same particle fragmentation strength $\sigma_c = 0.5 \cdot 10^3 P_0$.

behavior. On the other hand, in under-static states ($i_r < 1$), the number of constraints is insufficient to fully restrict the degrees of freedom of the particles, making the system mechanically unstable. This instability can progress and possibly culminate in liquefaction. Fig. 10 shows the variation of i_r with the shear strain. A decrease in i_r is observed as particle fragmentation strength decreases and, similarly, there is a greater and faster decrease associated with lower sample densities. This corroborates the previous sharp drop in pressure and coordination number that effectively reached states of liquefaction.

Let us now compare structural stability with macromechanical resistance. Fig. 10(b) shows the relationship between the redundancy number and the deviatoric stress. Interestingly, while all three densities

studied eventually exhibit states with $i_r < 1.0$, not all states lead to liquefaction. In other words, a redundancy number below 1 does not necessarily indicate zero shear resistance in the material. Liquefaction is observed for $i_r < 0.9$. Additionally, a higher particle fragmentation strength contributes to a high shear resistance and, consequently, higher redundancy numbers. As illustrated by the red dashed-dotted line in Fig. 10(b), it is possible to construct a master curve showing an exponential relationship between resistance values and redundancy numbers of the form $q \propto e^{\alpha i_r}$ in all the cases studied. We found a value of $\alpha = 22 \pm 3$ in our virtual tests. This finding suggests that, regardless of sample density and particle strength, the decrease in shear resistance relative to the redundancy ratio follows a quasi-unique path.
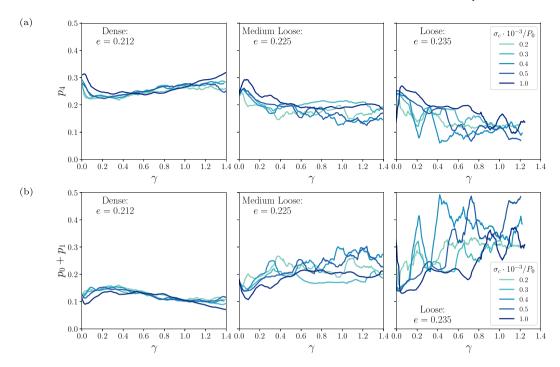
Fig. 9. Probability of having (a) four contacts, and (b) both zero and one contact (rattler), as a function of the shear strain for the three densities.
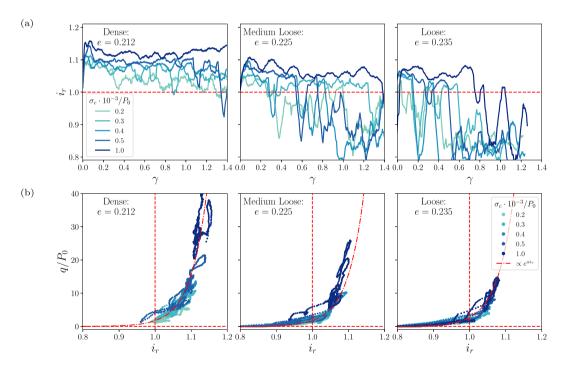

Fig. 10. (a) Redundancy number as a function of shear strain for three different initial densities and five particle fragmentation strength levels. The horizontal dashed red line indicates the threshold between solid-like and liquid-like mechanical behavior, with the redundancy index $i_r = 1$. (b) Deviatoric stress scaled by the initial compaction pressure as a function of the redundancy number for three different densities and five levels of particle fragmentation strength. The horizontal and vertical dashed red lines signals $q = 0$ and $i_r = 1$ respectively. Additionally, the red dashed-dotted line represents an exponential fit of the trend across all cases.

5. Particle crushing and grading evolution

The process of grain crushing significantly influences the liquefaction potential by continuously altering the size and shape of the crushed fragments. Fig. 11 illustrates this transformation, showing the cumulative distribution of particle sizes as a function of the shear strain, for a fragmentation strength of $\sigma_c = 0.5 \cdot 10^3 P_0$. In this figure, the particle size is defined by an effective diameter derived from the grain area, as their shapes are no longer circular after fragmentation. Initially, the particles

have a uniform size distribution with a slight polydispersity, ranging between d_{max} and d_{min}. As shearing progresses, grading asymptotically evolves towards the numerical ultimate state, where all grains in the packing have completely fragmented into their smallest numerical cell components. This ultimate cumulative size distribution, represented by the dashed red lines in Fig. 11, accounts for all polygonal cells resulting from the centroidal Voronoi tessellation of the initial circular particles (i.e., all the cell components), as explained in Section 2. Medium-loose and loose samples show a slower progression towards this ultimate
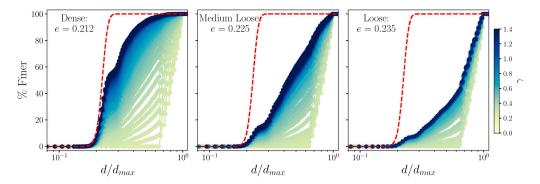
Fig. 11. Cumulative size distribution for the three densities studied at a particle fragmentation strength of $\sigma_c = 0.5 \cdot 10^3 P_0$. Colors range from yellow to blue, indicating increasing levels of shear strain. Additionally, the dashed red line indicates the ultimate possible grading, where all particles in the packing have fragmented down to their minimal numerical unit.
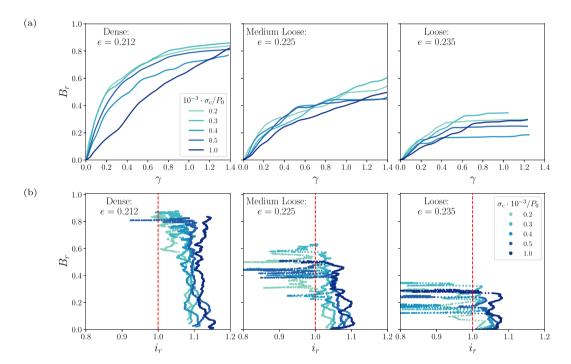

Fig. 12. (a) Modified Hardin breakage index as a function of shear strains for three different densities and particle stiffness. (b) Breakage index versus redundancy number for the same density and fragmentation strength conditions. The dashed red line indicates $i_r = 1$.

crushed state, suggesting that they experience less fragmentation under the same strain levels. As discussed in Section 3, a higher amount of particle crushing in denser samples generates more angular fragments, which explains the higher shear resistance in the denser cases shown in Fig. 5.

The degree of fragmentation is quantified using a modified Hardin breakage index (B_r) (Einav, 2007), which is determined by the relative position of the current cumulative grain size distribution ($F(d)$) in relation to both the initial grading ($F_0(d)$) and the ultimate grading ($F_u(d)$, red dashed line in Fig. 11), and is computed as:

$$B_r = \frac{\int_{d_{min}}^{d_{max}} \left(F(d) - F_0(d) \right) d^{-1} \, dd}{\int_{d_{min}}^{d_{max}} \left(F_u(d) - F_0(d) \right) d^{-1} \, dd} \quad (3)$$

Fig. 12(a) illustrates the evolution of the modified Hardin breakage index as a function of shear strain in all the samples studied. Generally, we observe a rapid initial increase in B_r for all samples. The evolution of the index asymptotically approaches a critical value at large strains, which is proportional to the packing density. This can be understood

by the fact that, with less available voids for the particles to rearrange, the only possible path to keep up upon shearing at constant volume is increasing the internal stresses, causing many particles to reach the fracture limit earlier. In contrast, lower-density samples exhibit a more dispersed range of critical breakage indices, with values more sensitive to particle fragmentation strength as the void ratio increases. These heterogeneities on grading at large strain have their origin in the instabilities in the internal stresses due to liquefaction, where fragmented particles exhibit a wide range of sizes and shapes

When observing the breakage index in dense samples, the ultimate grading appears to be independent of the particle fragmentation strength, converging to a similar value. However, σ_c becomes more important in loose samples, where the critical breakage value shows a significant dispersion, suggesting a strong dependency. Looking in more detail at B_r and its contribution to structural instabilities, Fig. 12(b) shows this factor as a function of the redundancy number. The structural instabilities, where $i_r < 1$, are observed to occur at values proportional to the ratio of voids and the strength of the particles.

Therefore, there is no universal breakage index threshold that triggers liquefaction.

6. Conclusions

In this paper, we investigate the mechanisms underlying the Sliding Surface Liquefaction (SSL) phenomenon through 2D virtual tests using the Discrete Element Method (DEM). The numerical approach enables the modeling of grain crushing through arbitrary fracture planes within solid particles, capturing size effects and varying grain fragmentation strengths across different samples. The assemblies of crushable grains were prepared in three different initial void ratios: dense, medium-loose and loose. The samples were subjected to simple shear paths at constant volume, with shear strains exceeding 1 and using periodic boundary conditions.

In the denser sample composed of the strongest particles, we observed dilative-type behavior, with effective stresses increasing drastically at high strains. However, reducing particle fragmentation strength and/or density led to strain softening. In all of the loose samples, as well as medium-loose samples with relatively low grain fragmentation strength, this behavior resulted in liquefaction, characterized by a complete loss of shear resistance. It is well known that these observations are due to particle crushing under constant volume shearing, which promotes contractive-like behavior, and consequently a further decrease in effective stresses. As a result, density plays a crucial role in determining the occurrence of liquefaction, as widely studied in the literature. However, here we also highlight the impact of particle fragmentation strength and initial stress, both captured by the ratio σ_c/P_0. Lowering this ratio can precipitate the onset of liquefaction, even in relatively dense cases. Despite variations in particle strength and density, grading always tends towards an ultimate distribution at large shear strains. Since dense samples generally undergo more crushing than loose ones, the amount of grain fragmentation does not directly correlate with the occurrence of liquefaction.

By focusing our observations on different scales, our study clearly showed the impact of grain crushing on the microstructure of the material undergoing liquefaction. However, several perspectives of this research can be drawn. For instance, analyses of 3D samples could exhibit drastically different particle rearrangement mechanisms and more contractive tendency after crushing, due to the additional degree of freedom that enlarges the possibilities for fragmented grains to fill the material voids. More realistic particle shapes and fragmentation models can also be implemented numerically, to consider grain anisotropy, as typically observed in metamorphic and sedimentary rocks. These simulations can also include rock weathering through diffusion and corrosion models, capturing delayed grain fragmentation and creep that might explain landslides triggered by static liquefaction. These features could also be suitable for the detection and study of shear bands in SSL behavior, which were not observed in our tests. Moreover, imposing constant volume we assumed that effective stresses are homogeneous in a sheared sample before liquefaction. However, in physical tests on saturated crushable samples, excess pore pressure could be localized within shear bands, resulting in heterogeneous fields of stresses and strains, which could impact the evolution of particle crushing. In future numerical research, this phenomenon could be addressed by using coupled Computational Fluid Dynamics (CFD) with DEM. This type of analysis, although computationally very expensive, could be compared with experimental results and provide tools to model the real behavior of field materials. Nevertheless, we anticipate that the fundamental mechanisms and the effects of density and grain strength will align with the findings of our study.

CRediT authorship contribution statement

Manuel Cárdenas-Barrantes: Writing – review & editing, Writing – original draft, Visualization, Validation, Software, Methodology, Investigation, Formal analysis, Conceptualization. **Carlos Ovalle:** Writing – review & editing, Writing – original draft, Visualization, Validation, Supervision, Resources, Project administration, Methodology, Investigation, Funding acquisition, Formal analysis, Conceptualization.

Declaration of Generative AI and AI-assisted technologies in the writing process

During the preparation of this work the authors used ChatGPT in order to improve the readability of the text.

Declaration of competing interest

All authors declare that they have no known competing financial interests or personal relationships that could have appeared to influence the work reported in this manuscript.

Data availability

Data will be made available on request.

References

Alonso, E.E., 2021. Triggering and motion of landslides. Geotech. 71 (1), 3–59. http://dx.doi.org/10.1680/jgeot.20.RL.001, arXiv:https://doi.org/10.1680/jgeot.20.RL.001, Retrieved from https://doi.org/10.1680/jgeot.20.RL.001.

ASTM, 2019. D8296-19: Standard test method for consolidated undrained cyclic direct simple shear test under constant volume with load control or displacement control. ASTM Int. 13. http://dx.doi.org/10.1520/D8296-19, Retrieved from https://www.astm.org/d8296-19.html.

Åström, J.A., Herrmann, H.J., 1998. Fragmentation of grains in a two-dimensional packing. Eur. Phys. J. B - Condens. Matter Complex Syst. 5 (3), 551–554. http://dx.doi.org/10.1007/s100510050476, Retrieved from https://doi.org/10.1007/s100510050476.

Bathurst, R.J., Rothenburg, L., 1988. Micromechanical aspects of isotropic granular assemblies with linear contact interactions. J. Appl. Mech. 55 (1), 17–23. http://dx.doi.org/10.1115/1.3173626, Retrieved from https://doi.org/10.1115/1.3173626.

Biarez, J., Hicher, P.-Y., 1997. Influence de la granulométrie et de son évolution par ruptures de grains sur le comportement mécanique de matériaux granulaires. Rev. Franc Caise de Genie Civ. 1 (4), 607–631. http://dx.doi.org/10.1080/12795119.1997.9692147.

Bruno Andeotti, Y.F., Pouliquen, O., 2013. GRANULAR MEDIA, Between Fluid and Solid. Cambridge University Press, London.

Cantor, D., Ovalle, C., Azéma, E., 2022. Microstructural origins of crushing strength for inherently anisotropic brittle materials. Int. J. Solids Struct. 238, 111399. http://dx.doi.org/10.1016/j.ijsolstr.2021.111399, Retrieved from https://www.sciencedirect.com/science/article/pii/S0020768321004601.

Carrasco, S., Cantor, D., Ovalle, C., Quiroz-Rojo, P., 2023. Shear strength of angular granular materials with size and shape polydispersity. Open Geomech. 4, 1–14. http://dx.doi.org/10.5802/ogeo.15, Retrieved from https://opengeomechanics.centre-mersenne.org/articles/10.5802/ogeo.15/.

Chen, Z., He, S., 2020. Simulation of effects of particle breakage on sliding surface friction for a hypothetical soil continuum moving on an inclined plane. Landslides 17 (9), 2113–2124. http://dx.doi.org/10.1007/s10346-020-01404-8, Retrieved from https://doi.org/10.1007/s10346-020-01404-8.

Coop, M.R., Sorensen, K.K., Bodas Freitas, T., Georgoutsos, G., 2004. Particle breakage during shearing of a carbonate sand. Geotech. 54 (3), 157–163. http://dx.doi.org/10.1680/geot.2004.54.3.157, arXiv:https://doi.org/10.1680/geot.2004.54.3.157, Retrieved from https://doi.org/10.1680/geot.2004.54.3.157.

Cui, S., Pei, X., Jiang, Y., Wang, G., Fan, X., Yang, Q., Huang, R., 2021. Liquefaction within a bedding fault: Understanding the initiation and movement of the Daguangbao landslide triggered by the 2008 Wenchuan earthquake (Ms=8.0). Eng. Geol. 295, 106455. http://dx.doi.org/10.1016/j.enggeo.2021.106455, Retrieved from https://www.sciencedirect.com/science/article/pii/S001379522100466X.

Daouadji, A., Darve, F., Al Gali, H., Hicher, P.Y., Laouafa, F., Lignon, S., Nicot, F., Nova, R., Pinheiro, M., Prunier, F., Sibille, L., Wan, R., 2011. Diffuse failure in geomaterials: Experiments, theory and modelling. Int. J. Numer. Anal. Methods Geomech. 35 (16), 1731–1773. http://dx.doi.org/10.1002/nag.975, arXiv:https://onlinelibrary.wiley.com/doi/pdf/10.1002/nag.975, Retrieved from https://onlinelibrary.wiley.com/doi/abs/10.1002/nag.975.

Dawson, R.F., Morgenstern, N.R., Stokes, A.W., 1998. Liquefaction flowslides in rocky mountain coal mine waste dumps. Can. Geotech. J. 35 (2), 328–343. http://dx.doi.org/10.1139/t98-009, arXiv:https://doi.org/10.1139/t98-009, Retrieved from https://doi.org/10.1139/t98-009.

de Bono, J.P., McDowell, G.R., 2018. Micro mechanics of drained and undrained shearing of compacted and overconsolidated crushable sand. Geotech. 68 (7), 575–589. http://dx.doi.org/10.1680/jgeot.16.P.318, arXiv:https://doi.org/10.1680/jgeot.16.P.318, Retrieved from https://doi.org/10.1680/jgeot.16.P.318.

Deng, Y., Fan, X., Scaringi, G., Wang, D., He, S., 2023. Effect of particle crushing–and thermally induced pressurization on rockslide mobility. Landslides 20 (7), 1535–1546. http://dx.doi.org/10.1007/s10346-023-02053-3, Retrieved from https://doi.org/10.1007/s10346-023-02053-3.

Deng, N., Wautier, A., Thiery, Y., Yin, Z.-Y., Hicher, P.-Y., Nicot, F., 2021. On the attraction power of critical state in granular materials. J. Mech. Phys. Solids 149, 104300. http://dx.doi.org/10.1016/j.jmps.2021.104300, Retrieved from https://www.sciencedirect.com/science/article/pii/S0022509621000089.

Du, Q., Faber, V., Gunzburger, M., 1999. Centroidal voronoi tessellations: Applications and algorithms. SIAM Rev. 41 (4), 637–676. http://dx.doi.org/10.1137/S0036144599352836, arXiv:https://doi.org/10.1137/S0036144599352836, Retrieved from https://doi.org/10.1137/S0036144599352836.

Dubois, F., Acary, V., Jean, M., 2018. The contact dynamics method: A nonsmooth story. C. R. Mec. 346 (3), 247–262. http://dx.doi.org/10.1016/j.crme.2017.12.009, Retrieved from https://www.sciencedirect.com/science/article/pii/S163107211730236X, The legacy of Jean-Jacques Moreau in mechanics / L'héritage de Jean-Jacques Moreau en mécanique.

Dubois, F., Jean, M., 2003. LMGC90 une plateforme de développement dédiée à la modélisation des problèmes d'interaction. In: Actes du sixieme colloque national en calcul des structures. Vol. 1, pp. 111–118.

Dubois, F., Jean, M., Renouf, M., Mozul, R., Martin, A., Bagneris, M., 2011. Lmgc90. In: 10e colloque national en calcul des structures. pp. Clé–USB.

Einav, I., 2007. Breakage mechanics—Part I: Theory. J. Mech. Phys. Solids 55 (6), 1274–1297. http://dx.doi.org/10.1016/j.jmps.2006.11.003, Retrieved from https://www.sciencedirect.com/science/article/pii/S0022509606001827.

Gerolymos, N., Gazetas, G., 2007. A model for grain-crushing-induced landslides—Application to Nikawa, Kobe 1995. Soil Dyn. Earthq. Eng. 27 (9), 803–817. http://dx.doi.org/10.1016/j.soildyn.2007.01.003, Retrieved from https://www.sciencedirect.com/science/article/pii/S0267726107000188.

Hawley, P.M., Cunning, J., 2017. Guidelines for Mine Waste Dump and Stockpile Design. CRC Press, London.

Hong, Y., Ling, X., He, K., 2021. Effects of sliding liquefaction on homogeneous loess landslides in western China. Sci. Rep. 11 (1), 11941. http://dx.doi.org/10.1038/s41598-021-91411-z, Retrieved from https://doi.org/10.1038/s41598-021-91411-z.

Hu, W., Hicher, P.-Y., Scaringi, G., Xu, Q., Van Asch, T.W.J., Wang, G., 2018. Seismic precursor to instability induced by internal erosion in loose granular slopes. Geotech. 68 (11), 989–1001. http://dx.doi.org/10.1680/jgeot.17.P.079, arXiv:https://doi.org/10.1680/jgeot.17.P.079, Retrieved from https://doi.org/10.1680/jgeot.17.P.079.

Huillca, Y., Silva, M., Ovalle, C., Quezada, J.C., Carrasco, S., Villavicencio, G.E., 2021. Modelling size effect on rock aggregates strength using a dem bonded-cell model. Acta Geotech. 16 (3), 699–709. http://dx.doi.org/10.1007/s11440-020-01054-z, Retrieved from https://doi.org/10.1007/s11440-020-01054-z.

Hyodo, M., Wu, Y., Aramaki, N., Nakata, Y., 2017. Undrained monotonic and cyclic shear response and particle crushing of silica sand at low and high pressures. Can. Geotech. J. 54 (2), 207–218. http://dx.doi.org/10.1139/cgj-2016-0212, arXiv:https://doi.org/10.1139/cgj-2016-0212, Retrieved from https://doi.org/10.1139/cgj-2016-0212.

Ishihara, K., 1996. Soil Behaviour in Earthquake Geotechnics. Clarendon Press, London.

Ishikawa, T., Miura, S., 2011. Influence of freeze-thaw action on deformation-strength characteristics and particle crushability of volcanic coarse-grained soils. Soils Found. 51 (5), 785–799. http://dx.doi.org/10.3208/sandf.51.785, Retrieved from https://www.sciencedirect.com/science/article/pii/S0038080620300858.

Kikumoto, M., Wood, D.M., Russell, A., 2010. Particle crushing and deformation behaviour. Soils Found. 50 (4), 547–563. http://dx.doi.org/10.3208/sandf.50.547, Retrieved from https://www.sciencedirect.com/science/article/pii/S0038080620302407.

Kokusho, T., Hara, T., Hiraoka, R., 2004. Undrained shear strength of granular soils with different particle gradations. J. Geotech. Geoenvironmental Eng. 130 (6), 621–629. http://dx.doi.org/10.1061/(ASCE)1090-0241(2004)130:6(621).

Kruyt, N.P., 2010. Micromechanical study of plasticity of granular materials. C. R. Mec. 338 (10–11), 596–603. http://dx.doi.org/10.1016/j.crme.2010.09.005.

Lade, P.V., Yamamuro, J.A., Bopp, P.A., 1996. Significance of particle crushing in granular materials. J. Geotech. Eng. 122 (4), 309–316. http://dx.doi.org/10.1061/(ASCE)0733-9410(1996)122:4(309).

Okada, Y., Sassa, K., Fukuoka, H., 2004. Excess pore pressure and grain crushing of sands by means of undrained and naturally drained ring-shear tests. Eng. Geol. 75 (3), 325–343. http://dx.doi.org/10.1016/j.enggeo.2004.07.001, Retrieved from https://www.sciencedirect.com/science/article/pii/S0013795204001516.

Oldecop, L., Alonso, E., 2004. Testing Rockfill Under Relative Humidity Control. Geotech. Test. J. 27 (3), 269–278. http://dx.doi.org/10.1520/GTJ11847, arXiv:https://asmedigitalcollection.asme.org/geotechnicaltesting/article-pdf/27/3/269/7080905/10_1520_gtj11847.pdf, Retrieved from https://doi.org/10.1520/GTJ11847.

Osses, R., Majdanishabestari, K., Ovalle, C., Pineda, J., 2021. Testing and modelling total suction effects on compressibility and creep of crushable granular material. Soils Found. 61 (6), 1581–1596. http://dx.doi.org/10.1016/j.sandf.2021.09.006, Retrieved from https://www.sciencedirect.com/science/article/pii/S0038080621001414.

Ovalle, C., Dano, C., 2020. Effects of particle size–strength and size–shape correlations on parallel grading scaling. Geotech. Lett. 10 (2), 191–197. http://dx.doi.org/10.1680/jgele.19.00095, arXiv:https://doi.org/10.1680/jgele.19.00095, Retrieved from https://doi.org/10.1680/jgele.19.00095.

Ovalle, C., Dano, C., Hicher, P.-Y., Cisternas, M., 2015. Experimental framework for evaluating the mechanical behavior of dry and wet crushable granular materials based on the particle breakage ratio. Can. Geotech. J. 52 (5), 587–598. http://dx.doi.org/10.1139/cgj-2014-0079, arXiv:https://doi.org/10.1139/cgj-2014-0079, Retrieved from https://doi.org/10.1139/cgj-2014-0079.

Ovalle, C., Hicher, P.-Y., 2020. Modeling the effect of wetting on the mechanical behavior of crushable granular materials. Geosci. Front. 11 (2), 487–494. http://dx.doi.org/10.1016/j.gsf.2019.06.009, Retrieved from https://www.sciencedirect.com/science/article/pii/S1674987119301240, Grain Crushing in Geoscience Materials.

Peng, J., Zhuang, J., Wang, G., Dai, F., Zhang, F., Huang, W., Xu, Q., 2018. Liquefaction of loess landslides as a consequence of irrigation. Q. J. Eng. Geol. Hydrogeol. 51 (3), 330–337. http://dx.doi.org/10.1144/qjegh2017-098, arXiv:https://www.lyellcollection.org/doi/pdf/10.1144/qjegh2017-098, Retrieved from https://www.lyellcollection.org/doi/abs/10.1144/qjegh2017-098.

Pouragha, M., Wan, R., 2016. Onset of structural evolution in granular materials as a redundancy problem. Granul. Matter 18 (3), 38. http://dx.doi.org/10.1007/s10035-016-0640-2, Retrieved from https://doi.org/10.1007/s10035-016-0640-2.

Quey, R., Dawson, P., Barbe, F., 2011. Large-scale 3D random polycrystals for the finite element method: Generation, meshing and remeshing. Comput. Methods Appl. Mech. Engrg. 200 (17), 1729–1745. http://dx.doi.org/10.1016/j.cma.2011.01.002, Retrieved from https://www.sciencedirect.com/science/article/pii/S004578251100003X.

Radjai, F., 2008. Contact dynamics method. Eur. J. Environ. Civ. Eng. 12 (7–8), 871–900. http://dx.doi.org/10.1080/19648189.2008.9693052, arXiv:https://doi.org/10.1080/19648189.2008.9693052, Retrieved from https://doi.org/10.1080/19648189.2008.9693052.

Radjai, F., Jean, M., Moreau, J.-J., Roux, S., 1996. Force distributions in dense two-dimensional granular systems. Phys. Rev. Lett. 77, 274–277. http://dx.doi.org/10.1103/PhysRevLett.77.274, Retrieved from https://link.aps.org/doi/10.1103/PhysRevLett.77.274.

Sadrekarimi, A., Olson, S.M., 2010. Particle damage observed in ring shear tests on sands. Can. Geotech. J. 47 (5), 497–515. http://dx.doi.org/10.1139/T09-117, arXiv:https://doi.org/10.1139/T09-117, Retrieved from https://doi.org/10.1139/T09-117.

Sammis, C.G., Osborne, R.H., Anderson, J.L., Banerdt, M., White, P., 1986. Self-similar cataclasis in the formation of fault gouge. Pure Appl. Geophys. 124 (1), 53–78. http://dx.doi.org/10.1007/BF00875719, Retrieved from https://doi.org/10.1007/BF00875719.

Sassa, K., Fukuoka, H., Scarascia-Mugnozza, G., Evans, S., 1996. Earthquake-induced-landslides: Distribution, motion and mechanisms. Soils Found. 36, 53–64. http://dx.doi.org/10.3208/sandf.36.Special_53, Retrieved from https://www.sciencedirect.com/science/article/pii/S0038080620329929.

Sassa, K., Fukuoka, H., Wang, G., Ishikawa, N., 2004. Undrained dynamic-loading ring-shear apparatus and its application to landslide dynamics. Landslides 1 (1), 7–19. http://dx.doi.org/10.1007/s10346-003-0004-y, Retrieved from https://doi.org/10.1007/s10346-003-0004-y.

Shi, D., Cao, D., Xue, J., Deng, Y., Liang, Y., 2022. DEM studies on the effect of particle breakage on the critical state behaviours of granular soils under undrained shear conditions. Acta Geotech. 17 (11), 4865–4885. http://dx.doi.org/10.1007/s11440-022-01580-y, Retrieved from https://doi.org/10.1007/s11440-022-01580-y.

Turcotte, D.L., 1986. Fractals and fragmentation. J. Geophys. Research: Solid Earth 91 (B2), 1921–1926. http://dx.doi.org/10.1029/JB091iB02p01921, arXiv:https://agupubs.onlinelibrary.wiley.com/doi/pdf/10.1029/JB091iB02p01921, Retrieved from https://agupubs.onlinelibrary.wiley.com/doi/abs/10.1029/JB091iB02p01921.

Voivret, C., Radjaï, F., Delenne, J.-Y., El Youssoufi, M.S., 2007. Space-filling properties of polydisperse granular media. Phys. Rev. E 76, 021301. http://dx.doi.org/10.1103/PhysRevE.76.021301, Retrieved from https://link.aps.org/doi/10.1103/PhysRevE.76.021301.

Wang, F., Sassa, K., 2000. Relationship Between Grain Crushing And Excess Pore Pressure Generation Of Sandy Soils In Ring-Shear Tests. Vol. All Days.

Wang, F., Sassa, K., Wang, G., 2002. Mechanism of a long-runout landslide triggered by the august 1998 heavy rainfall in Fukushima prefecture, Japan. Eng. Geol. 63 (1), 169–185. http://dx.doi.org/10.1016/S0013-7952(01)00080-1, Retrieved from https://www.sciencedirect.com/science/article/pii/S0013795201000801.

Wang, Z., Wang, G., 2022. Effect of particle breakage-induced frictional weakening on the dynamics of landslides. Granul. Matter 24 (3), 72. http://dx.doi.org/10.1007/s10035-022-01234-6, Retrieved from https://doi.org/10.1007/s10035-022-01234-6.

Wei, J., 2022. Particle-void fabric and effective stress reduction in cyclic liquefaction of granular soils. Soil Dyn. Earthq. Eng. 153, 107081. http://dx.doi.org/10.1016/j.soildyn.2021.107081, Retrieved from https://www.sciencedirect.com/science/article/pii/S0267726121005030.

Wood, D.M., Kikumoto, M., Russell, A., 2009. Prediction and Simulation Methods for Geohazard Mitigation. CRC Press, London, p. 6.

Yan, K., Wang, F., Liu, W., Zhang, B., Gao, J., 2023. Two long-runout rock avalanches in 2022 and 2020 in an underground coal mining field in Zhijin, China. Landslides 20 (7), 1465–1480. http://dx.doi.org/10.1007/s10346-023-02063-1, Retrieved from https://doi.org/10.1007/s10346-023-02063-1.

Yang, J., Yin, Z.-Y., Laouafa, F., Hicher, P.-Y., 2019. Analysis of suffusion in cohesion-less soils with randomly distributed porosity and fines content. Comput. Geotech. 111, 157–171. http://dx.doi.org/10.1016/j.compgeo.2019.03.011, Retrieved from https://www.sciencedirect.com/science/article/pii/S0266352X19300801.

Yin, Y., Li, B., Wang, W., Zhan, L., Xue, Q., Gao, Y., Zhang, N., Chen, H., Liu, T., Li, A., 2016. Mechanism of the december 2015 catastrophic landslide at the shenzhen landfill and controlling geotechnical risks of urbanization. Eng. 2 (2), 230–249. http://dx.doi.org/10.1016/J.ENG.2016.02.005, Retrieved from https://www.sciencedirect.com/science/article/pii/S209580991630950X.

Zhang, W., Rothenburg, L., 2020. Comparison of undrained behaviors of granular media using fluid-coupled discrete element method and constant volume method. J. Rock Mech. Geotech. Eng. 12 (6), 1272–1289. http://dx.doi.org/10.1016/j.jrmge.2020.03.009.

Zhou, C., Huang, W., Ai, D., Xu, H., Yuan, J., Kou, L., Luo, X., 2022. Catastrophic landslide triggered by extreme rainfall in Chongqing, China: July 13, 2020, Niuerwan landslide. Landslides 19 (10), 2397–2407. http://dx.doi.org/10.1007/s10346-022-01911-w, Retrieved from https://doi.org/10.1007/s10346-022-01911-w.